

Adiabatic and diabatic dynamics in the photodissociation of CH₂BrCl

Peng Zou, W. Sean McGivern and Simon W. North*

Department of Chemistry, Texas A&M University, P.O. Box 30012, College Station, TX 77842, USA. E-mail: north@mail.chem.tamu.edu

Received 30th May 2000, Accepted 6th July 2000

Published on the Web 4th August 2000

The photodissociation dynamics of chlorobromomethane (CBM) were investigated between 193 and 242 nm by resonance-enhanced multiphoton ionization (REMPI) with time-of-flight mass spectrometry (TOFMS). Translational energy distributions, anisotropy parameters, and Br : Br* branching ratios were determined at 193 and 235 nm to explore the non-adiabatic dynamics near the avoided crossing. Additional measurements were made at intermediate wavelengths to characterize the wavelength dependence of the Br and Br* anisotropy parameters. The non-adiabatic crossing probabilities calculated by applying a one-dimensional Landau–Zener model were relatively insensitive to the excitation wavelength, indicating that the avoided crossing between 3A' and 4A' potentials lies in the exit channel. Additionally, we have determined the partial absorption cross sections for the excited states that contribute to the ultraviolet absorption spectrum of CBM.

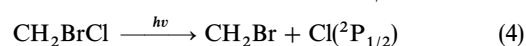
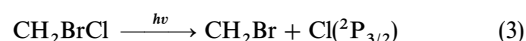
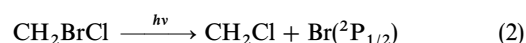
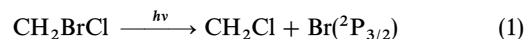
Introduction

The photodissociation dynamics of alkyl bromides have become the subject of significant study in recent years primarily because bromine atoms are estimated to be 40 times as efficient as chlorine atoms at destroying stratospheric ozone on an atom-for-atom basis.^{1,2} Investigations of monohalogen alkyl photodissociation are numerous and have revealed that non-adiabatic curve crossing dynamics play an important role in the ultraviolet photodissociation of these compounds. There are three electronic excited states that contribute to the first UV absorption band of CH₃X (X = Cl, Br and I) systems labeled ³Q₁, ³Q₀ and ¹Q₁.³ Among these states, only the ³Q₀ state diabatically correlates to X(²P_{1/2}) + CH₃, while the ³Q₁ and ¹Q₁ states correlate to X(²P_{3/2}) + CH₃ products. Amatatsu *et al.* have shown theoretically that for CH₃I photodissociation the molecular geometry in the region of the conical intersection has a strong effect on the observed product distribution,⁴ which is consistent with experimental studies.⁵ Similar behavior has been observed in the ultraviolet photodissociation of CH₃Br.^{6–8}

In contrast to monohalogen alkyl compounds, however, there have been relatively few investigations of multihalogen alkyl halides. Attempts to understand the effects of the substitution of halogen atoms have focused on the measurement of quantum yields for the ground state and spin–orbit excited fragments. Godwin *et al.* measured $I(^2P_{1/2}) : I(^2P_{3/2})$ ratios for a number of halogenated compounds and, including other results, characterized the alkyl halides into “families” with similar dynamic features.⁹ Based on the observed trends, the authors proposed that the substitution of an electronegative functionality shifted the location of the avoided crossing towards the exit channel. However, in the absence of measured product anisotropy parameters, it was assumed that only the ³Q₀ state was initially excited, making it unclear if the effects of the substitution were due to a shift in the location of the avoided crossing or a change in the nature of the initially excited electronic state(s). A more recent study on perfluorinated alkyl iodides by Kavita and Das¹⁰ found that the branching ratio of the perfluorinated species was too low to be explained by the model proposed by Godwin *et al.* Kavita

and Das concluded that the change in the branching ratio on fluorination could be due to low-frequency A' vibrations that couple the ¹Q₁ and ³Q₀ surfaces. However, anisotropy parameters were not measured, again calling the nature of the initial excited states into question.

In the present work, we have examined the photodissociation of chlorobromomethane (CBM) and have compared these results with those of CH₃Br to identify the effects of halogen substitution. There are four energetically allowed dissociation channels thought to contribute in this wavelength region for CBM:



Throughout this paper, we adopt the notation X and X* to describe the X(²P_{3/2}) and X(²P_{1/2}) products.

Multihalogenated alkanes with two different halogen atoms have lower intrinsic symmetry than their monohalogen analogues, resulting in a splitting of the degenerate ³Q₁ and ¹Q₁ excited states into [2A', 1A'] and [4A', 2A''] states, respectively. In the present paper, we use the notation [X, Y] to represent the formerly degenerate set of excited states resulting from the decrease in symmetry. In addition, the ³Q₀ excited state becomes 3A', and the ground state becomes 1A'. In C_s symmetry, the 3A' and 4A' components interact to form an avoided crossing. Measurement of the anisotropy parameters and X : X* branching ratios provides a means to examine and quantify the non-adiabatic dynamics in this region of the potential energy surfaces.

Photofragment translational spectroscopy (PTS) experiments by Tzeng *et al.* on the photodissociation of CBM at 193 and 248 nm suggested that the dissociation occurs on a repulsive surface following a predominately parallel transition at both wavelengths.¹¹ Although the PTS experiments were unable to resolve the individual ground state and excited state products, the observed marginal dependence of the anisotropy

parameters with respect to wavelength implied that the nature of the initially excited electronic states remained relatively constant. However, more recent work by our group on the photodissociation of CBM from 248 to 267 nm revealed that anisotropy parameters for the Br loss channel had a distinct wavelength dependence.¹² The calculated curve crossing probabilities in this wavelength region were found to be similar to those observed for CH₃Br^{6,7} after accounting for the differences in mass and geometry between CBM and CH₃Br.

We have reinvestigated the photodissociation of CBM at shorter wavelengths in order to characterize the dissociation dynamics over the entire UV absorption band corresponding to the $n \rightarrow \sigma^*$ transition of the C–Br bond. The wavelength-dependent anisotropy parameters and product quantum yields have provided additional insight into the non-adiabatic curve crossing dynamics. Based on an analysis using a one-dimensional Landau–Zener description, the avoided crossing appears to occur far into the exit channel. In addition, using the wavelength-dependent quantum yields and anisotropy parameters for each channel, we have decomposed the UV absorption spectrum into individual contributions from the [2A', 1A''], 3A' and [4A', 2A''] excited electronic states. The deconvolution reveals a small contribution from the [2A', 1A''] states at long wavelengths and nearly equal contributions from the 3A' and [4A', 2A''] states centered near the absorption maximum.

Experimental

The experimental set-up has been described in detail elsewhere,¹² and only the general features are described here. A pulsed molecular beam of 5% CBM in ~1 atm He was collimated and intersected at right angles with one or two laser beams. In the one-color experiments, the dissociation/probe beam was the doubled output of a pulsed dye laser operating with Coumarin 480 dye. The dissociation wavelengths were chosen to coincide with closely spaced 2 + 1 resonance-enhanced multiphoton ionization (REMPI) transitions of Br at 233.68 nm (4p ²P_{3/2} → 6p ²P_{3/2}) and Br* at 235.21 nm (4p ²P_{1/2} → 6p ²S_{1/2}), and the product quantum yields were assumed to remain constant over the small wavelength difference. In the two-color experiments, the output of an excimer laser operating on the ArF transition was counterpropagated with the pulsed dye laser beam running Coumarin 500 dye. A pile-of-plates polarizer was used to polarize the 193 nm excimer beam, and the reported anisotropy parameters have been corrected for the incomplete polarization. Br and Br* photofragments were detected in the two-color experiments by 2 + 1 REMPI transitions at 266.64 (4p ²P_{3/2} → 5p ⁴P_{3/2}) and 266.70 nm (4p ²P_{1/2} → 5p ²D_{3/2}), respectively.¹³

The resulting ions were detected using a traditional two-stage Wiley–McLaren¹⁴ time-of-flight (TOF) mass spectrometer coupled with a set of dual Chevron microchannel plates (MCP). In order to increase the velocity resolution, a copper plate with a 3 mm diameter pinhole was placed in the flight tube, allowing only those ions with small velocities perpendicular to the detection axis to strike the MCP.^{15–17} The core-sampling set-up has been described previously,¹⁸ but the present work represents the first application of the core-sampling technique on this apparatus to determine translational energy distributions for polyatomic molecules. The anisotropy parameters were determined in the absence of the coring aperture so that the anisotropy of the resulting spectra was dependent only on the shape of the TOF spectra and not on the relative intensities, which can be sensitive to slight changes in the overlap of the two beams. The MCP output was collected on a 400 MHz digital oscilloscope or a multi-channel scaler and was analyzed and archived on a PC. The REMPI scans were performed by recording boxcar-averaged MCP signals as a function of wavelength.

The CBM (99%) sample was purchased from Aldrich, and used without additional purification.

Results and analysis

In order to determine the quantum yields of Br and Br*, the individual REMPI detection efficiencies must be known. In the present work, the photodissociation of CH₃Br was studied, and the known Br : Br* branching ratio⁶ was used to calibrate the observed peak areas from a REMPI scan. The REMPI detection efficiencies of Br : Br* were previously determined to be 0.33 : 1 for the transitions near 267 nm.¹² In the present study, we find that the relative detection efficiency for Br : Br* is 0.46 : 1 for the transitions near 235 nm.

Forward convolution methods were developed to fit both non-cored and core-sampled data, and the non-cored TOF profile fitting procedure has been described in detail elsewhere.¹² The core-sampled TOF profile fitting procedure is similar, though restrictions are placed on the detected velocities due to the presence of the coring aperture. In core-sampling experiments, only fragments satisfying the following equation are detected:

$$(v^2 - v_z^2)^{1/2} t \leq a, \quad (5)$$

where v is the center-of-mass speed, v_z is the speed along the detection axis, t is the time required for a fragment to reach the coring aperture, and a is the radius of the coring aperture. Since the flight time is dependent on the velocity along the detection axis, v_z , this equation must be solved iteratively to obtain $v_{z, \max}$, the maximum v_z that can pass through the coring aperture for a specific center-of-mass velocity. In practice, a table of $v_{z, \max}$ values for each set of ion optic voltages was calculated for an entire center-of-mass velocity grid and archived. In order to fit the core-sampling TOF profile, a trial center-of-mass speed distribution, $g(v)$, of the form¹⁹

$$g(v) = \left(\frac{v}{v_{\max}} \right)^\alpha \left(1 - \frac{v}{v_{\max}} \right)^\beta,$$

where v_{\max} is the thermodynamic maximum velocity and α and β are adjustable parameters, was used to construct a trial velocity distribution, $f(v_z)$, subject to the previously determined $v_{z, \max}$ values. A Jacobian is applied to the TOF profile to account for the distortion of the ion packet in the field-free region. The $f(v_z)$ distributions are subsequently transformed to time-of-flight space, convolved with a Gaussian instrument response function (20 ns full width at half maximum (FWHM)), and compared with the experimental TOF spectra. The values of α and β are then iteratively adjusted to achieve the best fit.

Fig. 1 shows a core-sampled experimental TOF profile and forward convolution fit of the Br product at 224 nm. The broken lines represent the contributions to the TOF spectrum from the individual ⁷⁹Br and ⁸¹Br isotopes, and the solid line is the sum of these spectra to be compared with the experimental data. The translational energy distribution, $P(E_T)$, used to generate the fits to the present data are near-Gaussian in shape with FWHM of ~10 kcal mol⁻¹, consistent with a prompt dissociation process. Fig. 2 shows a TOF spectrum for Br* at 243 nm. As an example of the intensity changes on rotation of the polarization, we have included spectra taken at two experimental geometries, corresponding to the laser polarization taken vertical ($\chi = 0^\circ$) and horizontal ($\chi = 90^\circ$) to the detector axis. The solid line in Fig. 2 is a forward convolution fit of the experimental data using the method described above. The relative intensities of the fits give an anisotropy parameter, β , of 1.6 ± 0.2 . Shown in Fig. 3 are non-core-sampled TOF spectra for Br at 193 nm and their forward convolution fits (solid lines). As shown in Table 1, we obtain an average translational energy of 32 kcal mol⁻¹ with a state-

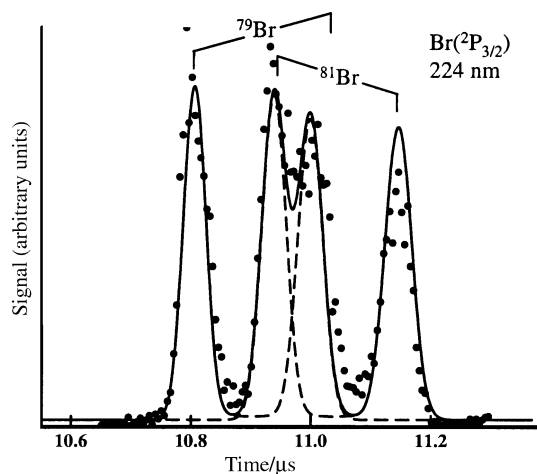


Fig. 1 Core-sampled Br TOF spectrum at 224 nm. Circles represent experimental data, and the solid line is the forward convolution fit. The broken lines show the individual contributions from the ^{79}Br and ^{81}Br isotopes.

averaged value of $31.5 \text{ kcal mol}^{-1}$, in good agreement with the results of Tzeng *et al.*¹¹ The FWHM of the $P(E_T)$ distributions for both Br and Br* are similar and are also found to be in good agreement with the translational energy distribution reported by Tzeng *et al.* As discussed in the Experimental section, we believe that a fit to the non-core-sampled TOF spectra provides a more accurate determination of the anisot-

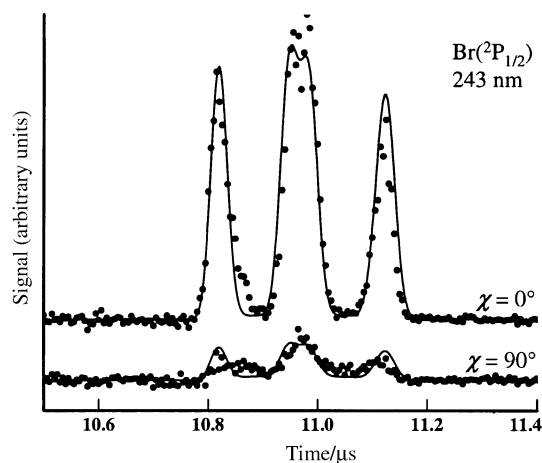


Fig. 2 Core-sampled Br* TOF spectra at 243 nm. Circles represent experimental data, and the solid lines are the forward convolution fits. The angle between the photolysis laser polarization and detector axis, χ , is indicated for each spectrum.

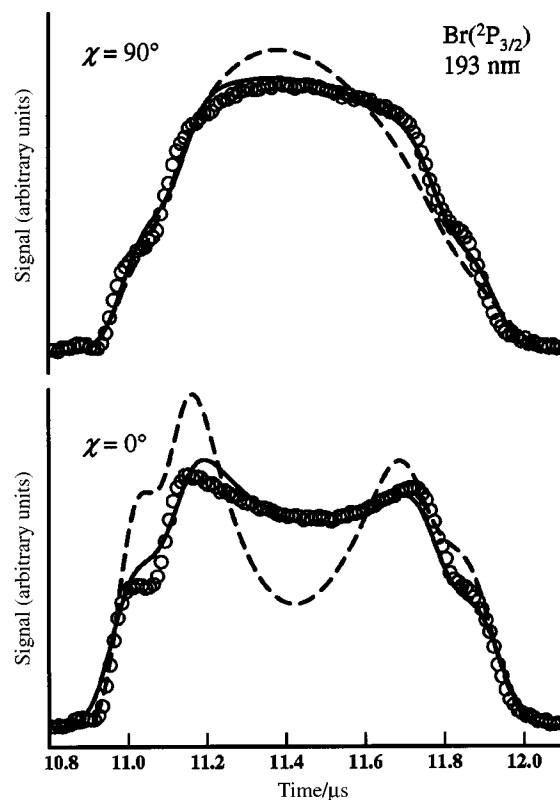


Fig. 3 Non-core-sampled Br TOF spectra at 193 nm. The angle between the photolysis laser polarization and detector axis, χ , is indicated for each spectrum. The solid lines represent a forward convolution fit with an anisotropy parameter of 0.53. The broken lines show a fit using an anisotropy parameter of 1.2, as suggested in ref. 11.

ropy parameter, because it depends only on the shape of the horizontal and vertical profiles and not on their relative intensities. However, anisotropy parameters determined using the relative intensities from core-sampled TOF spectra were fully consistent with the non-core-sampled results and within the cited error bounds. The values of the anisotropy parameters at 193 nm for both Br and Br* are inconsistent with the previously measured state-averaged anisotropy parameter of Tzeng *et al.* of 1.2.¹¹ The broken lines in Fig. 3 show fits at both geometries assuming a $P(E_T)$ distribution identical with that determined from the data with an anisotropy parameter of 1.2. For this anisotropy, the vertical TOF spectrum would show a significantly larger decrease at the slowest center-of-mass velocities than was observed. The origin of this discrepancy is unclear. The measured anisotropy parameters as a function of wavelength are shown in Fig. 4 and include data from our previous CBM photodissociation study.¹²

Table 1 Total translational energies, anisotropy parameters, and quantum yields in the ultraviolet photodissociation of CBM at several photolysis wavelengths

λ/nm	$E_{\text{avail}}/\text{kcal mol}^{-1}$	$\langle E_{\text{trans}} \rangle/\text{kcal mol}^{-1}$	$\frac{E_{\text{trans}}}{E_{\text{avail}}}$	β	Quantum yield
Br					
193	80.3	32 ± 1	0.40	0.53 ± 0.10	0.82 ± 0.10
234	54.6	29 ± 1	0.53	0.73 ± 0.10	0.80 ± 0.10
248 ^a	47.7	22 ± 1	0.46	1.1 ± 0.1	0.86 ± 0.10
266.7 ^a	39.6	24 ± 1	0.60	0.7 ± 0.1	0.91 ± 0.10
Br*					
193	69.8	29 ± 1	0.42	0.49 ± 0.20	0.18 ± 0.10
235	44.1	24 ± 1	0.55	1.3 ± 0.2	0.20 ± 0.10
248 ^a	37.2	20 ± 1	0.53	1.5 ± 0.2	0.14 ± 0.10
266.7 ^a	29.1	20 ± 1	0.68	1.4 ± 0.2	0.09 ± 0.10

^a Ref. 12.

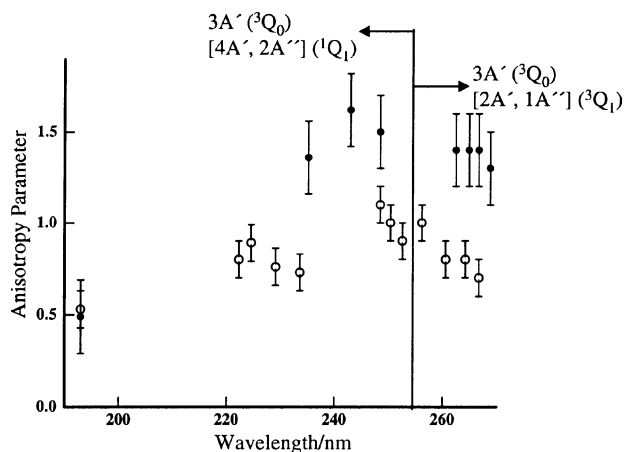


Fig. 4 Wavelength-dependent anisotropy parameters for the photolysis of CBM from 193 to 267 nm. The open circles represent Br anisotropy parameters and the closed circles are Br*. Photolysis in the shorter wavelength region is dominated by the $3A'$ (3Q_0) and $[4A', 2A'']$ (1Q_1) states, but the $[2A', 1A'']$ (3Q_1) state becomes much more significant at wavelengths longer than 248 nm.

The observed anisotropy parameter, β , is a measure of the orientation of the transition dipole moment with respect to the recoil velocity in the limit of prompt dissociation. In the axial recoil limit, $\beta = 2$ when the transition dipole is aligned parallel to the recoil direction and, $\beta = -1$ when the transition dipole is perpendicular to the recoil direction. The observed anisotropy parameter may then be considered a linear combination of these two limiting cases. For the ultraviolet photodissociation of CBM, there are five excited electronic states, $2A'$, $1A''$, $3A'$, $4A'$ and $2A''$, that are optically coupled to the ground state. Among them, only the $1A'' \rightarrow 3A'$ transition has a transition dipole moment parallel to the C–Br bond.¹² The $3A'$ state diabatically correlates to Br* products, but an avoided crossing between the $3A'$ and $4A'$ states is present in C_s symmetry which results in an adiabatic correlation of the $3A'$ state to Br and the $4A'$ state to Br* products. The remaining states correlate adiabatically to ground state products. The diabatic and adiabatic dynamics may be effectively examined because any parallel contribution to the Br* anisotropy parameter must be derived from a non-adiabatic crossing from the $3A'$ state. The non-adiabatic curve crossing probability, P , at a given dissociation wavelength may be determined by

$$P = \frac{\alpha_{\parallel}^{\text{Br}^*} \Phi_{\text{Br}^*}}{a_{\parallel}^{\text{Br}^*} \Phi_{\text{Br}^*} + a_{\parallel}^{\text{Br}} \Phi_{\text{Br}}}, \quad (6)$$

where a_{\parallel}^i 's and Φ_i 's are the normalized parallel contributions and quantum yields for the product channel containing halogen i , respectively. The measured anisotropy parameters and branching ratios are shown in Table 1 in addition to the crossing probabilities derived from these quantities.

Discussion

Ultraviolet absorption spectrum

The ultraviolet absorption spectrum of CBM²⁰ shows a broad peak with a maximum at ~ 202 nm, corresponding to an $n \rightarrow \sigma^*$ transition on the C–Br bond. A second peak begins to emerge at ~ 195 nm which is presumably due to an $n \rightarrow \sigma^*$ transition of the C–Cl bond. The absorption spectra of CH_3Br and CBM in the wavelength region between 195 and 270 nm are very similar, and the absorption onset for the C–Cl component of CBM corresponds closely to that of CH_3Cl .²¹ This suggests that the interaction between these two chromophores is probably minimal, and the electronic transitions and the

dynamics associated with the individual halogen loss channels may be studied independently.

In order to understand the excited states involved in the ultraviolet photodissociation of CBM, the absorption spectrum was deconvoluted into contributions from the $[2A', 1A'']$, $3A'$ and $[4A', 2A'']$ states. Individual Gaussian functions in energy were used to model the absorption from the three individual excited electronic states.²² Chlorine atoms were observed only at 193 nm, and the $n \rightarrow \sigma^*$ contribution of the C–Cl bond is very small even at this wavelength. A fourth Gaussian contribution to the absorption spectrum at wavelengths shorter than ~ 200 nm was included to account for this small contribution. By considering both the wavelength-dependent quantum yields of Br and Br* and the relative parallel and perpendicular contributions to each product channel, the excitation probabilities for each excited electronic state may be determined. The shapes and locations of the three Gaussian functions were adjusted until the relative contributions from each state reproduced the experimental absorption spectrum and gave the correct ratio of parallel to perpendicular contributions at each wavelength studied. Since both the $[2A', 1A'']$, and $[4A', 2A'']$ states may result in perpendicular bromine, we assume that the only perpendicular contribution at wavelengths longer than 248 nm comes from the $[2A', 1A'']$ state. As shown in Fig. 4, the Br* anisotropy parameters show little change within the experimental error from 267 to 248 nm, indicating that the electronic state from which the Br* product is derived is not changing. However, the Br component shows a clear increase with decreasing wavelength, indicating that the $3A'$ state is preferentially populated with increasing photolysis energy. A significant contribution from the $[4A', 2A'']$ state would tend to decrease the Br* anisotropy parameter with decreasing wavelength, which is not the observed trend. Therefore, the assumption that only the $[2A', 1A'']$ state contributes to the red-wing absorption appears to be reasonable. The resulting decomposition is shown in Fig. 5. The $[2A', 1A'']$ state is seen to make a very small contribution to the overall absorption band, though it plays a prominent role in the far red-wing dissociation dynamics (> 250 nm). The $3A'$ and $[4A', 2A'']$ states are very close in energy and have nearly equal widths, though the $3A'$ absorption is slightly broader and makes a significant contribution at longer wavelengths.

The deconvolution of the CBM absorption spectrum in this wavelength region shows a number of differences from previously reported partial absorption cross sections of CH_3Br .⁶ Both CBM and CH_3Br show relatively small contributions

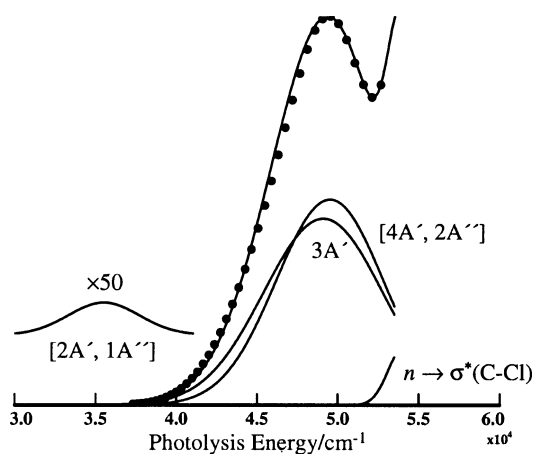


Fig. 5 Decomposition of ultraviolet absorption spectrum into three components which represent the $[2A', 1A'']$ (3Q_1), $3A'$ (3Q_0) and $[4A', 2A'']$ (1Q_1) states, respectively. A contribution from the $n \rightarrow \sigma^*(\text{C-Cl})$ excitation was included at large photolysis energies and closely corresponds to the CH_3Cl absorption onset.

from the lowest energy electronic states at long wavelengths, but the [2A', 1A''] state in CBM appears to be shifted to significantly longer wavelengths and makes a much smaller contribution. The 3Q_0 and 1Q_1 states also show a much larger energy difference than the corresponding 3A' and [4A', 2A''] states in CBM. However, the C–Br absorption spectra appear to be very similar, and the C–Br dissociation dynamics appear to be uncoupled from the C–Cl bond. Such a large change in the nature of the initially excited electronic states from CH₃Br is somewhat unexpected. In the decomposition of the CH₃Br absorption spectrum, Gougousi *et al.* do not make the assumption that the 3Q_1 state contributes only at the longest wavelengths and find a relatively large contribution from the 3Q_1 state in the red-wing of the absorption spectrum.⁶ Gedanken and Rowe have performed magnetic circular dichroism (MCD) experiments on methyl halides and note that the contribution from the 3Q_1 state of methyl iodide is extremely small.²³ A re-analysis of the MCD data based on a more realistic numerical model²⁴ found results consistent with the MCD experiments, showing only a 5% contribution from the 3Q_1 state of CH₃I. Amatatsu *et al.*⁴ have identified a 17% contribution from the 3Q_1 state using trajectory calculations on a nine-dimensional potential energy surface, which is consistent with previous experimental results.^{25,26} Since the spin-orbit coupling of methyl bromide is significantly smaller than in methyl iodide, both the 3Q_1 and 3Q_0 contributions in methyl bromide would be expected to decrease relative to the 1Q_1 state. The decomposition shown in Fig. 5 shows a very small [2A', 1A''] (equivalent to the 3Q_1 state in C_{3v} symmetry) component, and the 3A' (3Q_0) component has become nearly equal to the [4A', 2A''] (1Q_1) component. Though Gougousi *et al.*⁶ have shown a relatively large 3Q_1 component at long wavelengths for CH₃Br photodissociation, the qualitative features of the deconvolution shown in Fig. 5 are consistent with the expected behavior of the CH₃I partial absorption crossing sections with decreasing spin–orbit coupling.

Non-adiabatic dynamics

The non-adiabatic curve crossing probability, P , may be estimated by using a one-dimensional Landau–Zener expression

$$P = \exp\left(-\frac{\zeta}{v}\right) \quad (7)$$

where ζ is an adjustable parameter dependent on the splitting between adiabatic surfaces and the difference in the slopes of the potential surfaces at the avoided crossing, and v is the radial velocity at the avoided crossing. Although the Landau–Zener model neglects several degrees of freedom that may play an important role in photodissociation processes, its application can provide a qualitative understanding of the non-adiabatic dynamics. As shown in Table 1, the average translational energy increases approximately linearly with increasing photolysis energy. Though the intercept is clearly non-zero, the behavior of the translational energy for the wavelengths relevant to the present study is approximately in accord with the impulsive model. Therefore, we have chosen to estimate the radial velocity in the region of the avoided crossing by assuming that the asymptotic translational energy may be determined from a linear fit. The location of the avoided crossing may then be estimated by fitting the observed curve crossing probabilities to eqn. (7) as a function of the radial velocity and the adjustable parameter ζ . The best fit to the wavelength-dependent non-adiabatic curve crossing probability strongly suggests that the energy of the avoided crossing is located in the exit channel, though the simplifications present in the Landau–Zener model preclude a more quantitative analysis. At such a curve crossing, the radial velocity at the point of crossing is relatively insensitive to the photolysis wavelength, and, as a consequence, only weakly

affects the curve crossing probability. If the crossing point were located at a significantly higher energy, a dramatic change in the crossing probability would be expected as a function of the photolysis wavelength for energies near the crossing point.

Godwin *et al.* have measured $I^* : I$ branching ratios for the photodissociation of a large number of alkyl and halogenated alkyl iodides at 248 nm.⁹ The molecules were categorized into “families” based on the assumption that the locations of the avoided crossings, the non-adiabatic couplings, and the differences in the slopes of the potentials for each molecule were dependent only on the chemical environment surrounding the α -carbon. The authors assumed that only the 3Q_0 state is populated during the photolysis, and based on observed changes in the $I : I^*$ branching ratios, proposed that the substitution of an electronegative moiety on the α -carbon shifts the curve crossing towards the exit channel. Though the assumption that the 3Q_0 state is exclusively populated at 248 nm is not severe in CH₃I,²⁷ anisotropy parameters were not measured for any of the molecules studied. Therefore, it is unclear whether the approximation holds for the entire class of molecules studied.²⁸ More recently, Kavita and Das measured I^* quantum yields for the photodissociation of per-fluorinated alkyl iodides at 266, 280 and 305 nm.¹⁰ The quantum yields measured by Kavita and Das were significantly lower than the values expected from a Landau–Zener analysis using the ζ values measured by Godwin *et al.* The authors proposed a different explanation in which the low-frequency components were believed to couple the 1Q_1 and 3Q_0 surfaces more effectively in the fluorinated compound. However, like the Godwin *et al.* study, anisotropy parameters were not measured, and the nature of the initially excited electronic states for each molecule remains unclear. Studies measuring anisotropy parameters, translational energy distributions, and product branching ratios as a function of wavelength are necessary to obtain a firm understanding of the effects of halogen substitution on a photodissociation process.

Conclusions

The photodissociation of CBM between 193 and 242 nm has been studied using resonance enhanced multiphoton ionization coupled with a TOF mass spectrometer. We have presented a method of analysis for the fitting of core-sampled TOF data and used it to derive translational energy distributions for each photodissociation channel. Non-adiabatic curve crossing probabilities were calculated by measuring anisotropy parameters and product quantum yields at both 193 and 235 nm. Using these results, we have decomposed the UV absorption spectrum into the sum of four Gaussian functions, representing the [2A', 1A''], 3A', and [4A', 2A''] electronic states, which correspond to C–Br bond dissociation, and a small contribution from the $n \rightarrow \sigma^*$ transition of the C–Cl bond. A one-dimensional Landau–Zener analysis based on the measured translational energy distributions strongly suggests that the 3A' \rightarrow 4A' avoided crossing is located in the exit channel.

Acknowledgements

The authors thank Professor Bruce Johnson for his helpful comments. We also acknowledge the technical assistance of Trieu Nguyen during these experiments. This work was supported by a Research Enhancement Grant from Texas A&M University.

References

- 1 F. S. Rowland, *Annu. Rev. Phys. Chem.*, 1991, **42**, 731.
- 2 S. C. Wofsy, M. B. McElroy and Y. L. Yung, *Geophys. Res. Lett.*, 1975, **2**, 215.

- 3 R. S. Mulliken, *Phys. Rev.*, 1942, **61**, 277.
- 4 Y. Amatatsu, S. Yabushita and K. Morokuma, *J. Chem. Phys.*, 1996, **104**, 9783.
- 5 E. Hirota, *Annu. Rev. Phys. Chem.*, 1991, **42**, 1 and references cited therein.
- 6 T. Gougousi, P. C. Samartzis and T. N. Kitsopoulos, *J. Chem. Phys.*, 1998, **108**, 5742.
- 7 J. G. Underwood and I. Powis, *Phys. Chem. Chem. Phys.*, 2000, **2**, 747.
- 8 G. N. A. Van Veen, T. Baller and A. E. De Vries, *Chem. Phys.*, 1985, **92**, 59.
- 9 F. G. Godwin, P. A. Gorry, P. M. Hughes, D. Raybone, T. M. Watkinson and J. C. Whitehead, *Chem. Phys. Lett.*, 1987, **135**, 163.
- 10 K. Kavita and P. K. Das, *J. Chem. Phys.*, 2000, **112**, 8426.
- 11 W. B. Tzeng, Y. R. Lee and S. M. Lin, *Chem. Phys. Lett.*, 1994, **227**, 467.
- 12 W. S. McGivern, R. Li, P. Zou and S. W. North, *J. Chem. Phys.*, 1999, **111**, 5771.
- 13 S. Arepalli, N. Presser, D. Robie and R. J. Gordon, *Chem. Phys. Lett.*, 1985, **117**, 64.
- 14 W. C. Wiley and I. H. McLaren, *Rev. Sci. Instrum.*, 1955, **26**, 1150.
- 15 R. Ogarzalek-Loo, J.-P. Haerri, G. E. Hall and P. L. Houston, *J. Chem. Phys.*, 1989, **90**, 4222.
- 16 H. J. Hwang, J. Griffiths and M. A. El-Sayed, *Int. J. Mass Spectrom. Ion Processes*, 1994, **131**, 265.
- 17 J. A. Syage, *J. Chem. Phys.*, 1996, **105**, 1007.
- 18 W. S. McGivern, R. Li, P. Zou, T. Nguyen and S. W. North, *Chem. Phys.*, 1999, **249**, 237.
- 19 S. W. North, A. J. Marr, A. Furlan and G. E. Hall, *J. Phys. Chem., A*, 1997, **101**, 9224.
- 20 V. L. Orkin, V. G. Khamaganov, A. G. Guschin, R. E. Huie and M. J. Kurylo, *J. Phys. Chem. A*, 1997, **101**, 174.
- 21 W. B. DeMore, S. P. Sander, C. J. Howard, A. R. Ravishankara, D. M. Golden, C. E. Kolb, R. F. Hampson, M. J. Kurylo and M. J. Molina, *Chemical Kinetics and Photochemical Data for Use in Stratospheric Modeling*, Evaluation 12, Jet Propulsion Laboratory, Pasadena, CA, 1997.
- 22 E. U. Condon, *Phys. Rev.*, 1928, **32**, 858.
- 23 A. Gedanken and M. D. Rowe, *Chem. Phys. Lett.*, 1974, **34**, 39.
- 24 B. R. Johnson and J. L. Kinsey, *J. Phys. Chem.*, 1996, **100**, 18937.
- 25 R. A. Hertz and J. A. Syage, *J. Chem. Phys.*, 1994, **100**, 9625.
- 26 D. H. Fairbrother, K. A. Briggman, E. Weitz and P. C. Stair, *J. Chem. Phys.*, 1994, **101**, 3787.
- 27 A. T. J. B. Eppink and D. H. Parker, *J. Chem. Phys.*, 1998, **109**, 4758.
- 28 See, for example, W. E. Kang, K. W. Jung, K. H. Jung and H. J. Hwang, *J. Phys. Chem.*, 1994, **98**, 1525.